ARTICLES
https://doi.org/10.1038/s41560-018-0324-8
nature energy

Planar p–n homojunction perovskite solar cells with efficiency exceeding 21.3%

Peng Cui[1,4], Dong Wei[1,4], Jun Ji[1], Hao Huang[1], Endong Jia[2,3], Shangyi Dou[1], Tianyue Wang[1], Wenjing Wang[2,3] and Meicheng Li[1*]

Perovskite solar cells (PSCs) have emerged as an attractive photovoltaic technology thanks to their outstanding power conversion efficiency (PCE). Further improvement in the device efficiency is limited by the recombination of the charge carriers in the perovskite layer even when employing heterojunction-based architectures. Here, we propose and demonstrate a p-type perovskite/n-type perovskite homojunction whose built-in electric field promotes oriented transport of the photo-induced carriers, thus reducing carrier recombination losses. By controlling the stoichiometry of the perovskite precursors, we are able to induce n-type or p-type doping. We integrate the homojunction structure in a planar PSC combining a thermally evaporated p-type perovskite layer on a solution-processed n-type perovskite layer. The PSC with a $MAPbI_3$ homojunction achieves a PCE of 20.80% (20.5% certified PCE), whereas the PSC based on a $FA_{0.15}MA_{0.85}PbI_3$ homojunction delivers a PCE of 21.38%. We demonstrate that the homojunction structure is an effective approach, beyond existing planar heterojunction PSCs, to achieve highly efficient PSCs with reduced carrier recombination losses.

Organic–inorganic halide perovskite solar cells (PSCs) have attracted much interest thanks to their high power conversion efficiency (PCE)[1–5], which has increased from 3.8% up to 23.7% in less than 10 years[6,7], facile processing methods[8,9] and outstanding optoelectronic properties[10–15]. Many effective strategies have been implemented to improve the performance of PSCs, such as solvent engineering[16–18], compositional engineering[19,20] and alternative architecture design[21–23]. In particular, recent works[24–27] show that minimizing the carrier recombination losses, both in the perovskite layer and at the interfaces between different layers, enables a PCE closer to the theoretical value[1].

One strategy for reducing carrier recombination losses is to minimize defects on polycrystalline perovskite films[5,24,26]. For instance, additional iodide ions can be introduced into the organic cation solution, which decrease the concentration of the deep-level defects[5]. Another strategy is to engineer the device architecture employing mesoporous, planar or embedded structures to reduce the carrier losses during charge transport/extraction in PSCs[22,28,29]. Furthermore, the use of a bulk heterojunction active layer has been demonstrated to shorten the carrier transport distance in the perovskite films, thus reducing carrier losses[23,30,31]. Moreover, to decrease further the recombination losses and to improve the photoelectron collection, an inverted device architecture with a graded heterojunction structure has also been reported[32]. These results illustrate that improving the device architecture in heterojunction PSCs is a valid approach to decrease the carrier losses. While the heterojunction is constituted between the perovskite and electron/hole transport materials, the perovskite itself is also able to form a homojunction thanks to its unique self-doping property[33–37], which would minimize the presence of impurities that can act as carrier recombination centres[38]. Within the perovskite homojunction, a built-in electric field is formed that could enhance the oriented transport of the photo-induced electrons/holes, thus decreasing further carrier recombination in the perovskite layer. Therefore, it is a promising route to further improve the performances of PSCs.

Here, we fabricate a perovskite p–n homojunction structure, via a combined deposition processing method, which is then integrated into planar PSCs. The built-in electric field in the homojunction, identified by cross-sectional Kelvin probe force microscopy (KPFM), induces the oriented transport of the photo-induced carriers, thus reducing the carrier recombination losses as further corroborated by wxAMPs simulations. Planar PSCs with a $MAPbI_3$ (MA, methylammonium) p–n homojunction exhibit a steady-state efficiency of 20.80%. Furthermore, an average PCE of 21.38% is achieved by utilizing a $FA_{0.15}MA_{0.85}PbI_3$ (FA, formamidinium) p–n homojunction, exceeding the previously reported efficiency for planar PSCs.

Fabrication of the planar homojunction PSC

The proposed homojunction structure is composed of two perovskite layers with different doping, p-type and n-type perovskites, placed in junction with one another. A built-in electric field is therefore established at the p–n junction. Theoretical simulations and experimental evidence show that perovskites can be either p-type or n-type depending on the growth conditions and the ratio of the main precursors[33–37]. The $MAPbI_3$ films with Pb^{2+}-rich/MA^+-deficient/I^--deficient precursors are n-doped and those with MA^+-rich/Pb^{2+}-deficient precursors are p-doped, due to the presence of the defects induced by vacancies or interstitial elements. Previously, we have demonstrated that self-doping in perovskites can be tuned serially by controlling the process conditions, such as annealing temperatures[39,40]. Hence, it is feasible to fabricate a perovskite homojunction structure.

We integrate the homojunction into PSCs based on the standard planar p–i–n[41,42] structure (Au/spiro-OMeTAD/$MAPbI_3$/compact TiO_2/fluorine-doped tin oxide (FTO)). Schematic illustrations of PSCs with the standard p–i–n structure and the homojunction

[1]State Key Laboratory of Alternate Electrical Power System with Renewable Energy Sources, School of Renewable Energy, North China Electric Power University, Beijing, China. [2]Key Laboratory of Solar Thermal Energy and Photovoltaic System, Institute of Electrical Engineering, Chinese Academy of Sciences, Beijing, China. [3]University of Chinese Academy of Sciences , Beijing, China. [4]These authors contributed equally: Peng Cui, Dong Wei. *e-mail: mcli@ncepu.edu.cn

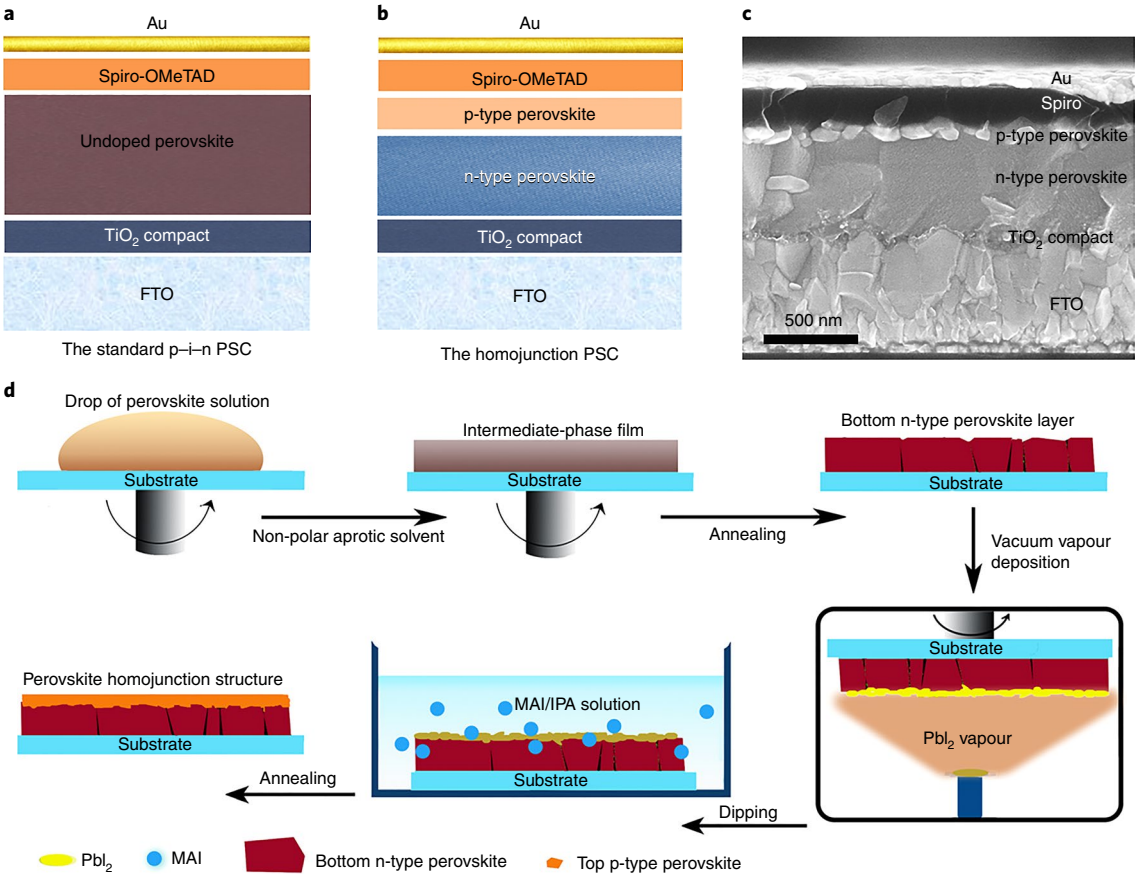

Fig. 1 | Structure of planar PSCs with and without the homojunction and fabrication schematic of the homojunction PSC fabricated by the combined deposition method. a, The standard p–i–n PSC without the homojunction. **b**, The PSC with the homojunction composed by p-type and n-type perovskite layers. **c**, A cross-sectional SEM image of a homojunction PSC. The thicknesses of the TiO_2, n-type perovskite, p-type perovskite, spiro-OMeTAD and Au electrode are about 20 nm, 480 nm, 60 nm, 200 nm and 100 nm, respectively. **d**, The bottom n-type perovskite layer is deposited by a one-step spin-coating method. The top p-type perovskite layer is deposited by vacuum vapour deposition followed by a dipping process.

structure are displayed in Fig. 1a,b. Figure 1c presents a cross-sectional scanning electron microscopy (SEM) image of a homojunction PSC, where a smooth and uniform n-type $MAPbI_3$ layer can be clearly observed. Meanwhile, the dense and small-grain p-type $MAPbI_3$ layer with a thickness of ~60 nm is deposited on the top of the ~480 nm n-type $MAPbI_3$ layer.

To realize the perovskite homojunction structure, we propose a combined deposition method that combines a one-step spin-coating method for the deposition of the bottom n-type perovskite layer on top of the TiO_2 compact layer and a vacuum vapour deposition followed by a dipping step for the deposition of the top p-type perovskite layer over the n-type perovskite layer.

The one-step spin-coating method allows control of the morphology, coverage, roughness and grain size of the n-type perovskite film. By varying the stoichiometry of the PbI_2/MAI precursor ratio (1, 1.05, 1.10 and 1.15, respectively), we are able to induce the n-type doping in the perovskite. The deposition of the top p-type perovskite layer of the homojunction should not degrade the bottom n-type perovskite layer. While spin-coating would dissolve the bottom layer, vacuum vapour deposition has been reported to avoid damage of the organic/inorganic thin films underneath while enabling high-quality films[22,43,44]. We therefore choose this technique for depositing PbI_2 thin films on top of the n-type perovskite layer, followed by a dipping step in MAI/isopropanol solution to form $MAPbI_3$. By adjusting the dipping time, we control the amount of MAI and thus the p-type doping. Finally, we choose the top p-type perovskite layer with a PbI_2 thickness of 60 nm followed by a dipping time of 60 s, whose precursor ratio is measured at ~0.91 (PbI_2/MAI). The SEM images, X-ray diffraction patterns and high-resolution transmission electron microscope images (Supplementary Note 1) of perovskite layers are shown in Supplementary Figs. 1–3, respectively.

Carrier generation and recombination in homojunction PSC

Figure 2a shows a schematic energy level diagram and the working principle of the homojunction PSC and how carriers are transported across the layers. As photons are absorbed by both the p-type and n-type perovskites, the photo-induced carriers are generated in two perovskite layers. Then, the electrons and holes at the homojunction drift in opposite directions. Finally, the electrons are injected into the compact TiO_2 layer, the electron transport layer (ETL), and transported to the FTO cathode whereas the holes are injected into the spiro-OMeTAD layer, the hole transport layer (HTL), and transported to the Au anode.

In PSCs with the standard p–i–n structure, the carrier transport in the perovskite film has no preferred direction, which can lead to unwanted carrier recombination. The extraction of photo-induced electrons and holes mostly occurs at the perovskite/ETL and the perovskite/HTL interfaces, respectively[27]. Hence, we design the homojunction structure to provide an extra built-in electric field in the perovskite film, in which electrons and holes move in opposite directions towards the ETL and the HTL, respectively, as shown in Fig. 2b, with a view to reducing carrier recombination.

To verify the reduction in carrier recombination losses, carrier generation and recombination in PSCs is simulated with wxAMPS,

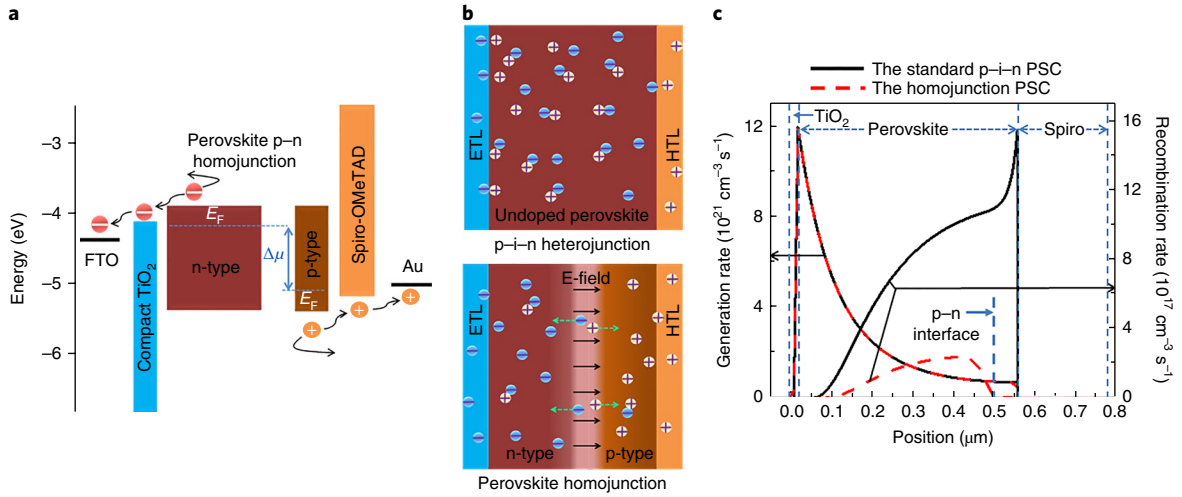

Fig. 2 | Carrier generation and recombination of the planar PSCs with and without the homojunction. a, An energy bandgap diagram of the homojunction PSC. E_F and $\Delta\mu$ represent the Fermi levels of the n-type and p-type perovskites and the Fermi level difference, respectively. Electrons (red circles) are transported through the n-type perovskite and collected at the FTO electrode. Holes (yellow circles) are transported through the p-type perovskite and collected at the Au electrode. **b**, Carrier generation and transport in PSCs with (bottom) and without (top) the homojunction. The solid black and dashed green arrows represent the built-in electric field direction and the carrier transport direction, respectively. The blue circles indicate electrons and the yellow circles indicate holes. The HTL and the ETL are shown in orange and blue, respectively. **c**, Simulated generation and recombination rates of the photo-induced carriers across PSCs on illumination (AM1.5G) and under short-circuit conditions. The position refers to the cross-sections of the homojunction PSC, TiO_2 (20 nm)/n-type perovskite (480 nm)/p-type perovskite (60 nm)/spiro-OMeTAD (200 nm), and the standard p–i–n PSC, TiO_2 (20 nm)/undoped perovskite (540 nm)/spiro-OMeTAD (200 nm), respectively. The dashed blue lines are used to identify the layers in the PSCs.

which has been used to simulate thin-film solar cells[39,45,46]. The simulated structures for these two PSCs are shown in Supplementary Fig. 4a. In Fig. 2c, under short-circuit conditions, the rates of carrier generation are similar for both devices whereas the carrier recombination rate for PSCs with the homojunction is dramatically reduced near the p-type/n-type perovskite interface. We suggest that this is due to the electric field (Supplementary Fig. 4b) induced by the homojunction that favours the oriented transport of electrons and holes. As a result of the influence of the homojunction, the concentration of the free holes increases in the p-type perovskite region away from the interface, whereas the concentration of the electrons decreases (Supplementary Fig. 4c,d), providing evidence for carrier oriented transport. Besides, the simulated photocurrent density–voltage *(J–V)* curve (Supplementary Fig. 5 and Supplementary Note 2) in the homojunction PSC shows an obvious enhancement in open-circuit voltage (V_{OC}).

Optoelectronic properties of the perovskite homojunction

To detect the doping property of as-prepared perovskite films, X-ray photoemission spectroscopy (XPS) is carried out on perovskite films with various contents of PbI_2 in precursor solution. The valence spectra and the schematic energy level of the perovskite films are shown in Fig. 3a,b. The energy difference between the valence band and the Fermi level (E_F) is 0.50 eV for the top p-type perovskite film with a PbI_2/MAI ratio of 0.91, which confirms the p-type doping due to the perovskite's bandgap of 1.55 eV. For the perovskite films containing excess PbI_2, the E_F is shifted close to the conduction band, with the increase in PbI_2 content in the precursor solution. This illustrates that the doping of the perovskite can be tuned from p-type to n-type by changing the PbI_2 content in the precursor solution. The full XPS spectra of the $MAPbI_3$ films are shown in Supplementary Fig. 6. The position of the XPS peaks, especially for I and Pb, does not vary across the samples, thus indicating that the changes in the valence spectra are due to the perovskite materials, not measurement errors. The doping of the films is also characterized by Hall effect measurements. As shown in Fig. 3c and Supplementary Table 1, the carrier transport type converts from p-type to heavily n-type with increasing molar ratios of PbI_2.

In addition, KPFM, which is employed to characterize the surface potentials, also confirms the results presented above. Figure 3d,e shows KPFM potential images of the p-type perovskite films with a PbI_2/MAI ratio of 0.91 and the n-type perovskite with a PbI_2/MAI ratio of 1.15 (other ratios are reported in Supplementary Fig. 7), respectively, whereas the insets show the atomic force microscope (AFM) topographic images. It can be seen from Fig. 3d that the surface potential of the p-type perovskite film is lower than that of the n-type perovskite film (Fig. 3e), because of accumulated holes that lead the Fermi level to be located close to the valence band[39]. Contrarily, the higher surface potential of the n-type perovskite film shown in Fig. 3e correlates with the n-type doping of the sample, which is consistent with the XPS and Hall results. To get a quantitative comparison, the profiles of the surface potentials of the films are compared in Fig. 3f. The surface potential on the n-type perovskite film is approximately 0.1 V whereas that of the p-type perovskite film is about −0.3 V.

The time-resolved photoluminescence (TRPL) and the steady PL measurements are performed for the single n-type perovskite film (PbI_2/MAI ratio of 1.15) and the perovskite homojunction film (n-type layer with a PbI_2/MAI ratio of 1.15 and p-type layer with PbI_2/MAI ratio of 0.91). As shown in Fig. 3g, TRPL decay of perovskite films showed a bi-exponential decay with a fast and a slow component. The bimolecular recombination rate, a, and the decay lifetime, τ, are estimated by fitting the decay curves with the expressions $I = I_0(1 + at)^{-2}$ and $I = I_0 \times \exp(-(t/\tau)^{\beta})$, respectively, and reported in the inset table of Fig. 3g. Previous studies of carrier recombination in perovskite films suggest that the fast decay process is caused by bimolecular recombination of photo-generated free carriers, whereas the slow decay process is attributed mainly to trap-assisted recombination[26,39]. Here, the perovskite homojunction film possesses a higher bimolecular recombination rate ($a = 2.9 \times 10^8\ s^{-1}$) and a shorter fast decay lifetime ($\tau_1 = 6.3$ ns) than the n-type perovskite film while the slow decay lifetime (τ_2) is

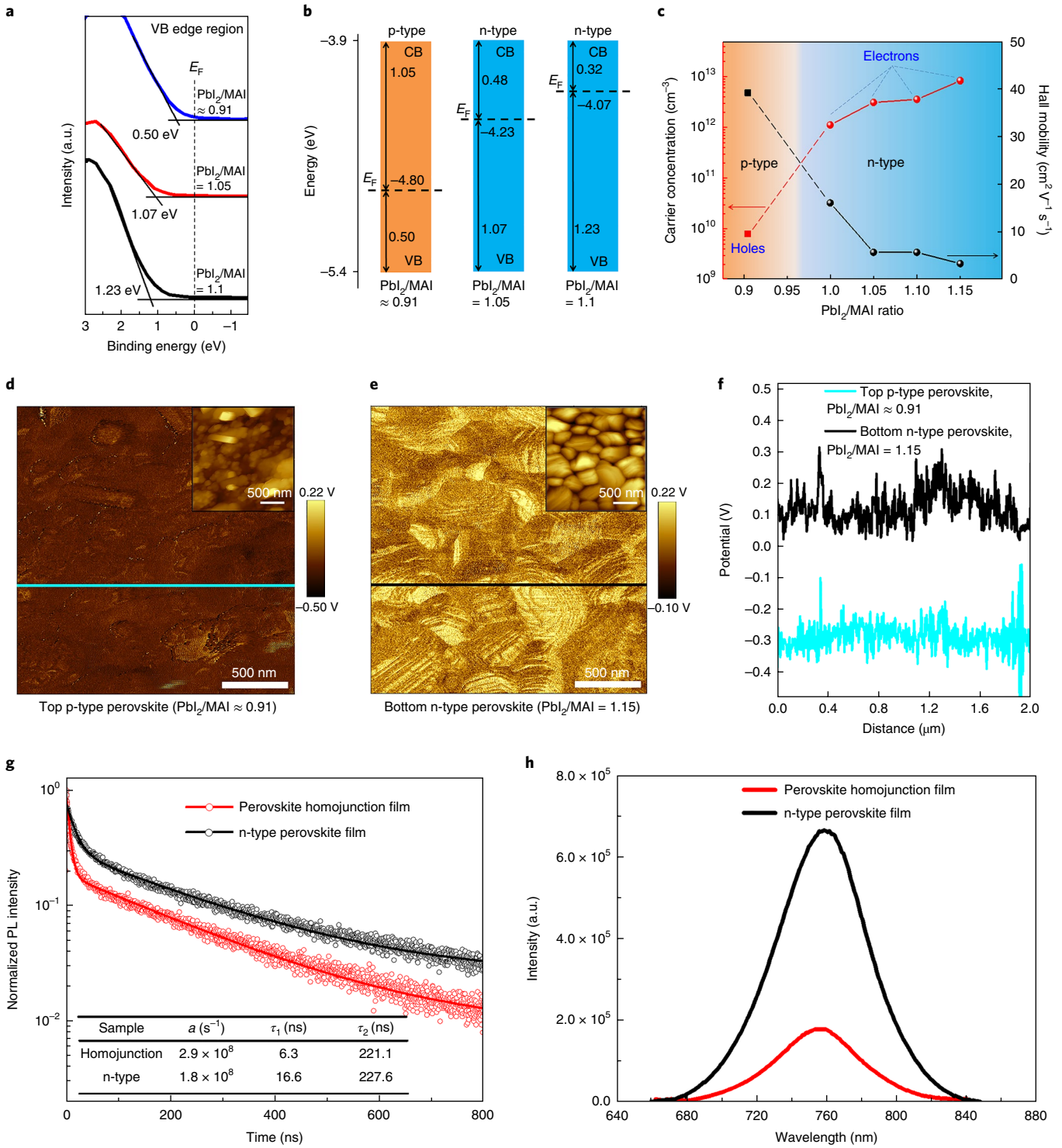

Fig. 3 | Doping, carrier transport and optical properties of the doped perovskite films. a, XPS valence spectra of $MAPbI_3$ films with different molar ratios of PbI_2/MAI. The ratio of 0.91 indicates the p-type perovskite whereas the ratios of 1.05 and 1.1 indicate n-type perovskites. **b**, The energetic levels of the corresponding n-type (blue) and p-type (orange) perovskite films. CB, conduction band; VB, valence band. **c**, The carrier concentration (red symbols) and mobility (black symbols) for electrons (circle) and holes (square) in the perovskite films extracted by Hall measurements. The area colours of orange and blue represent the p-type and n-type doping, respectively, for different PbI_2/MAI ratios. **d**,**e**, Surface potential maps (KPFM) of $MAPbI_3$ films; low surface potentials are found for the p-type perovskite with a PbI_2/MAI ratio of 0.91 (**d**) whereas high surface potentials are found for the n-type perovskite with a PbI_2/MAI ratio of 1.15 (**e**); the topography maps (AFM) of these two films are shown in the insets. The colour scale bar of the KPFM indicates the relative scale of the surface potential. The blue and black lines across the images (**d**,**e**) mark the locations to extract the potential profiles in **f**. **f**, Surface potential line profiles of the corresponding perovskite films (the blue line in **d** and the black line in **e**). **g**, TRPL decay profiles excited by a 485 nm pulse laser and measured at 760 nm for the FTO/n-type perovskite/PMMA and FTO/homojunction (n-type perovskite/p-type perovskite)/PMMA films. The values of the recombination rate (a) and the decay lifetime (τ_1 and τ_2) corresponding to the fast and slow decay component of these two films are estimated by fitting the TRPL decay curves and reported in the inset table. **h**, Steady PL spectra of n-type perovskite film (black line) and homojunction film (n-type perovskite/p-type perovskite, red line). In **g**,**h**, the n-type perovskite is from the PbI_2/MAI ratio of 1.15, whereas the p-type perovskite is from the PbI_2/MAI ratio of 0.91.

similar in the two samples. This indicates that efficient carrier transfer occurs between the two type perovskite layers in the homojunction without introducing more traps in the homojunction, possibly because of the built-in field at the p–n junction. PL spectra of these two films are consistent with the results of TRPL. As shown in Fig. 3h, the intensity of PL for the perovskite homojunction film is quenched by over 80% relative to that of the single n-type perovskite film, proving the efficient oriented transport of carriers between the n-type and p-type perovskite layers of the homojunction induced by the built-in potential, which can potentially enable higher performances in PSCs.

Evidence for the perovskite p–n homojunction formation

To further verify the formation of the p–n junction between the two perovskite layers, KPFM measurements have been performed on the cross-section of the homojunction structure under dark conditions, which can be used to study the electrical potential distribution across the internal interfaces in solar cells[37,47–49]. A schematic of the KPFM measurement principle is shown in Supplementary Fig. 8. We fabricate the homojunction device based on FTO/n-type perovskite/p-type perovskite/Au and we cleave it to expose the cross-section without applying any treatments (for example, polishing or ion milling) to avoid complications and artefacts. Moreover, to exclude the influence of surface charges (defects) created on the cleaved cross-sectional surface, we employ a method for measuring the potential changes based on a series of bias voltages (V_b) that are sufficiently small (from the −1.0 V to +0.5 V)[48,49]. We can obtain the obvious potential change caused by the transport and extraction of carriers at the junction, because the configuration of surface charges trapped at defects would not change significantly with such a small V_b (ref. [48]).

Figure 4a,b shows the AFM topography of the homojunction device and the corresponding KPFM potential image at $V_b = 0$, respectively. As shown in the potential profile in Fig. 4c, a potential drop is observed at the interface of the n-type/p-type perovskite layers caused by the carrier transport at the interface. This demonstrates the existence of a built-in electric field and thus the existence of the p–n junction. Besides, the dark and photoelectric J–V curves of homojunction devices show the typical rectifying characteristic of the p–n junction (Supplementary Fig. 9). Remarkably, this simple homojunction device composed of two perovskite layers and relative electrodes but without an HTL and an ETL exhibits a PCE of up to 8.08%, corroborating the presence of the p–n junction.

To obtain accurate information about the bulk property by cross-sectional potential measurements, we measured the potential changes on the same area induced by applying various V_b (Supplementary Fig. 10). The averaged line profiles of the potential under different V_b are shown in Fig. 4d. We subtract the $V_b = 0$ potential profile from the −1.0 V (reverse) up to the +0.5 V (forward) potential profiles, calculate the potential difference curves at the various V_b (Fig. 4e) and then take the first derivative of the curves to obtain electrical field differences (Fig. 4f).

In Fig. 4d, we note that the potential in the FTO changes slightly with the different V_b, even though the FTO is grounded. One reason could be the non-negligible resistance of FTO (~16 Ω sq^{-1}) and the contact resistance (~2 Ω), which act as series resistors with a voltage drop across them. Hence, the actual voltage applied on the homojunction is not the entire V_b. Another reason is that cleaving the sample cross-section would create shunts and decrease the shunt resistance, so the current under V_b is larger than that of a non-cleaved device under the same bias voltage[48,49]. In addition, we also check for possible topographic effects. The topography of the cross-section is not very smooth because of the restriction of the sample preparation without further treatment. We choose two line-scan potential profiles whose locations are across large particles in topography maps (Supplementary Fig. 11). Although the topographic height changes significantly, the potential along the two lines appears to have an almost identical distribution, therefore suggesting minimal crosstalk between the topography and KPFM potential measurements (Supplementary Note 3).

From the potential and field difference curves (Fig. 4e,f, respectively), the significant potential drops and the electric field enhancement are observed across the n-type/p-type perovskite interface. Moreover, the position of maximum electric field corresponds to the n-type/p-type perovskite boundary, indicating a junction at the interface. Due to the p–n junction characteristic, the potential change trends at the junction area are different under the forward and reverse V_b, and the electric field directions are also opposite under the forward and reverse V_b. Besides, we use the same method to measure the control device (FTO/TiO_2/undoped perovskite/spiro-OMeTAD/Au) (Supplementary Figs. 11 and 12). We observe a potential drop and a rise at the TiO_2/perovskite and the perovskite/spiro-OMeTAD interfaces, respectively, at $V_b = 0$. Under different bias voltages, two major electric fields are located across the two interfaces, which demonstrates that the control device works as a p–i–n junction as opposed to a homojunction device.

The homojunction-enhanced solar cell performance

To check the effects of the homojunction on the performance of PSCs, $MAPbI_3$-based and $FA_{0.15}MA_{0.85}PbI_3$-based perovskite layers are chosen for fabricating planar PSCs. The performances of PSCs with and without the homojunction are presented in Fig. 5. First, we fabricate the $MAPbI_3$ homojunction PSCs. The top p-type perovskite layer is fabricated with a PbI_2 thickness of 60 nm followed by a dipping time of 60 s (that corresponds to a PbI_2/MAI ratio of ~0.91) and the n-type perovskite layer (480 nm) is fabricated with a PbI_2/MAI ratio of 1.10. The performance-optimized results with the PbI_2 thickness for the top p-type perovskite and the self-doping concentration for the bottom n-type perovskite can be found in Supplementary Fig. 13. The perovskite layer in $MAPbI_3$ standard p–i–n PSCs is deposited by solution processing to a thickness of about 540 nm, similarly to that of the homojunction film as shown in Supplementary Fig. 1i,j. As shown in Fig. 5a, the performances of the champion $MAPbI_3$ PSCs with and without the homojunction are compared. The homojunction PSC exhibits a better performance than the standard p–i–n PSC with an increase in the PCE from 17.76% to 20.80%. Among the photovoltaic parameters, the short-circuit current density (J_{SC}) shows the greatest improvement, increasing from 22.54 mA cm^{-2} to 23.86 mA cm^{-2}. To understand the reason behind the J_{SC} increase, we measure the absorbance spectra of these perovskite films and the external quantum efficiency (EQE) of the corresponding PSCs. The absorption curves of these two perovskite films are similar, which indicates that the perovskite homojunction does not induce additional absorption (Supplementary Fig. 14a). The EQE spectra and the corresponding integrated J_{sc} estimated for the $MAPbI_3$ PSCs with and without the homojunction are shown in Supplementary Fig. 14b. The EQE of the homojunction PSC is higher than the standard p–i–n PSC, especially at long wavelengths (from 500 nm to 800 nm). The homojunction probably suppresses the carrier recombination. The integrated J_{SC} matches well with the measured J_{SC}. Hence, the notable increase in J_{SC}, V_{OC} and fill factor (FF) of the homojunction PSC is mainly attributed to the effective oriented transport of photo-generated carriers induced by the built-in field of the homojunction, which minimizes the loss in the photovoltaic performance. A 20.5% efficiency for the $MAPbI_3$ homojunction PSCs is certified by the National Institute of Metrology in China (Supplementary Fig. 15).

Besides, the stabilized electric power output and the photocurrent density at the maximum power point are measured over a period of 200 s and shown in Fig. 5b. By holding a bias near the maximum power output point (+0.95 V), we obtained a stabilized

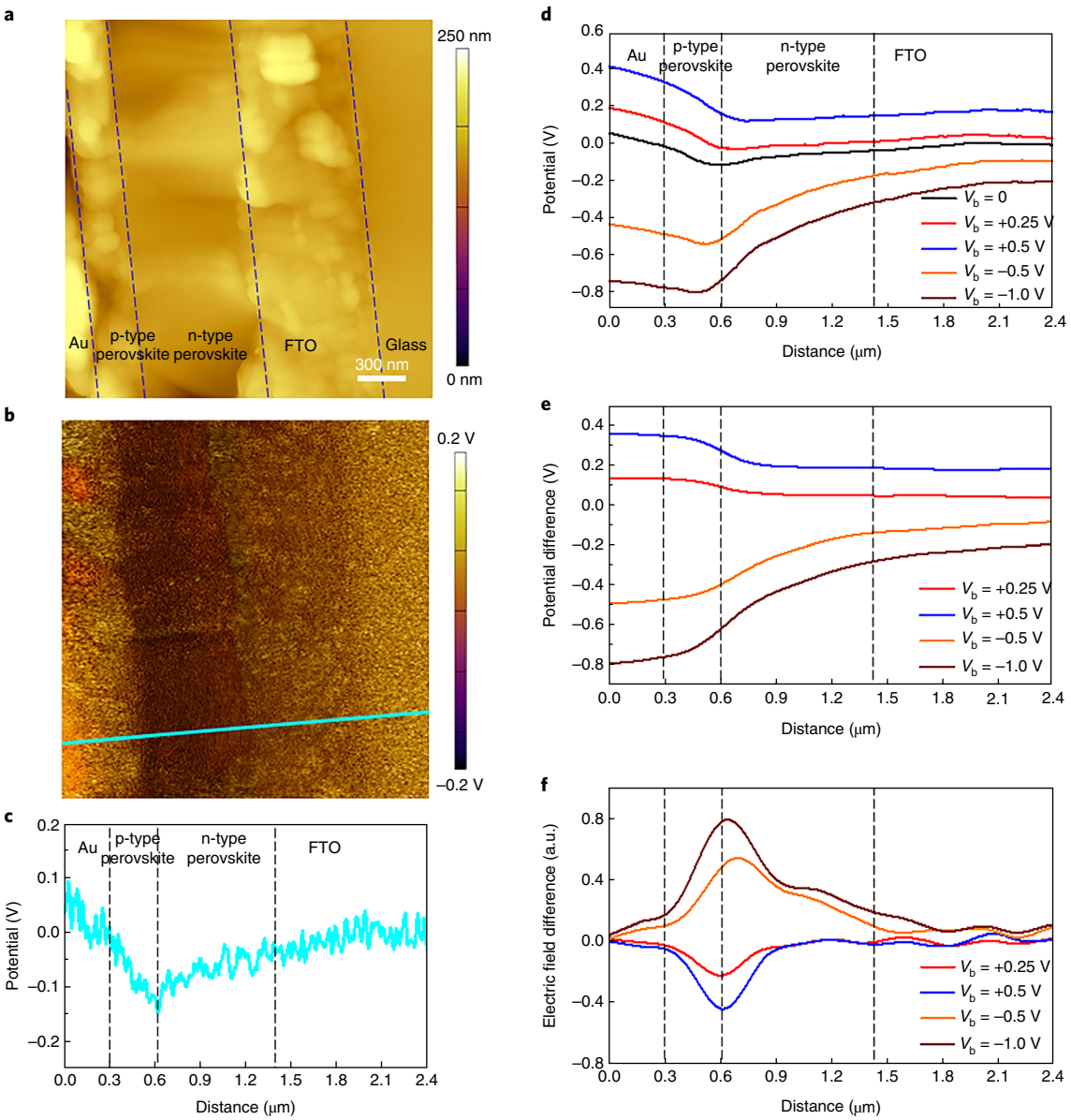

Fig. 4 | Cross-sectional KPFM measurement for the perovskite homojunction device under different bias voltages. a, AFM topography images of the device ($V_b = 0$). The dashed blue lines are used to identify the layers in the device. **b**, The corresponding KPFM images. The colour scale bars of the AFM and KPFM indicate the relative scales of the surface corrugation and the potential. The cyan line (**b**) marks the location to extract the potential profiles in **c**. **c**, The line scan potential profile along the cyan line in **b**. **d**, Potential profiles of the device under the various bias voltages. **e**, Potential difference profiles with respect to the $V_b = 0$. **f**, Electric field profiles under the various bias voltages. The potential profiles in **d** are averaged from the potential images along the device lateral direction. The potential differences in **e** are obtained by subtracting the potential under $V_b = 0$ from the potentials under the various V_b. The profiles of the electric field difference in **f** are deduced by taking a derivative of the potential differences in **e**. The device structure is FTO/homojunction (n-type perovskite/p-type perovskite)/Au. The dashed grey lines are used to identify the layers in the device in **c**–**f**. Furthermore, FTO (grounded) and Au are connected to a voltage source to realize different bias voltages (V_b) to the device.

PSC of ~20.6%, which is similar to the non-stabilized PCE of 20.80% measured for the same cell. As shown in Fig. 5c, the homojunction greatly improves the performance and reproducibility compared to the standard structure (other parameters are reported in Supplementary Fig. 16). The average PCE for 45 standard p–i–n PSCs is 15.92% with a J_{sc} of 22.27 mA cm^{-2}, V_{oc} of 1.06 V and FF of 67.20%. For the 45 homojunction PSCs, the average PCE reaches up to 19.95% with an average J_{sc} of 23.43 mA cm^{-2}, V_{oc} of 1.12 V and FF of 76.09%.

Hysteresis has frequently been observed in PSCs, so its assessment is important to evaluate the performance of PSCs accurately. We perform serial forward/reverse scanned J–V measurements on one of the most efficient $MAPbI_3$ homojunction PSCs to examine the influence of the biasing history. We observe little difference between the J–V curves measured under reverse and forward scans (Supplementary Fig. 17), which indicates that the doping of the perovskite for the homojunction within the stoichiometry explored in this work does not lead to significant hysteresis. We obtained a mean PCE of 20.1% from 8 measurements (Supplementary Table 2), based on the averaged values of the reverse and forward scanned J–V curves with the $MAPbI_3$ homojunction PSC. The discrepancy in the PCEs derived from the two scanned direction curves (that is, reverse and forward) is only 0.7%, revealing that the homojunction PSCs have small hysteresis.

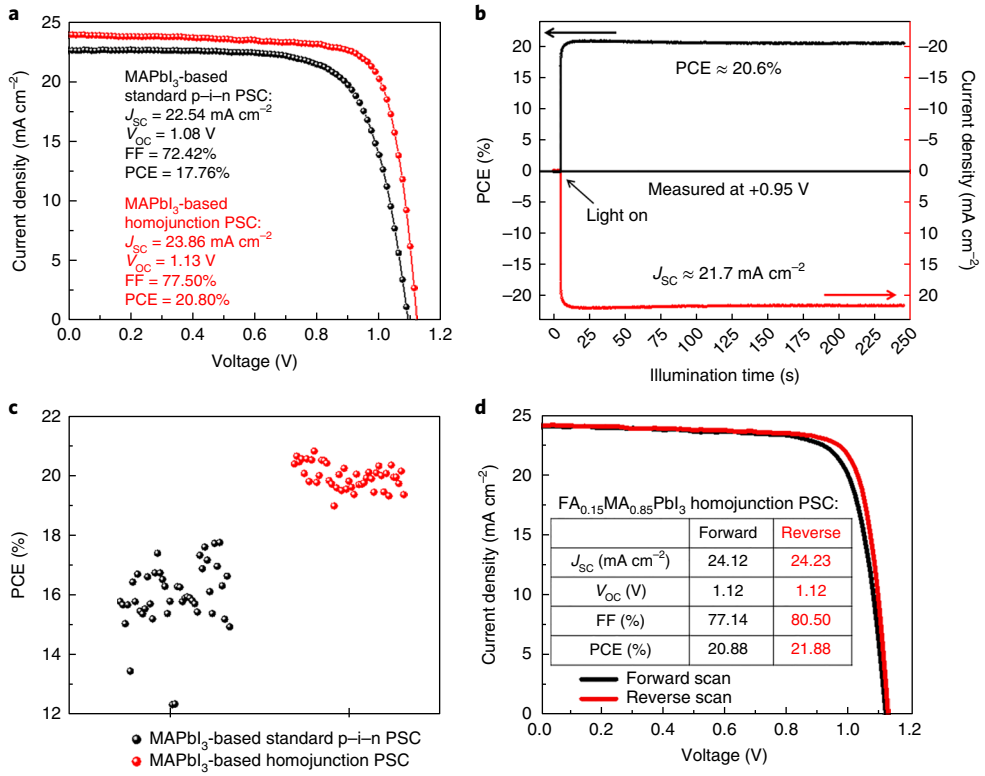

	Forward	Reverse
J_{SC} (mA cm^{-2})	24.12	24.23
V_{OC} (V)	1.12	1.12
FF (%)	77.14	80.50
PCE (%)	20.88	21.88

Fig. 5 | Photovoltaic performance of the planar PSCs with and without the homojunction. a, *J*–*V* curves (reverse scan) of the champion $MAPbI_3$ PSCs. **b**, Steady-state photocurrent and efficiency at the maximum power point (0.95 V) for the optimized $MAPbI_3$ homojunction PSC. **c**, PCEs of 45 $MAPbI_3$ standard p–i–n PSCs and 45 $MAPbI_3$ homojunction PSCs. **d**, *J*–*V* curves for the champion $FA_{0.15}MA_{0.85}PbI_3$ homojunction PSC.

To demonstrate the generalizability of the homojunction in PSCs, planar $FA_{0.15}MA_{0.85}PbI_3$ PSCs with and without the homojunction have been fabricated and tested. The *J*–*V* curves indicate that the performance of $FA_{0.15}MA_{0.85}PbI_3$ homojunction PSCs is improved markedly in terms of all the photovoltaic parameters as shown in Supplementary Fig. 18. Notably, the champion $FA_{0.15}MA_{0.85}PbI_3$ homojunction PSC shows a PCE of 21.88% with an FF of up to 80.50% under reverse scanning and a PCE of 20.88% under forward scanning, leading to an average PCE of 21.38% (as shown in Fig. 5d; the EQE and integrated J_{sc} are shown in Supplementary Fig. 19). We demonstrated that the performances are significantly improved when using the homojunction structure for planar $MAPbI_3$ or $FA_{0.15}MA_{0.85}PbI_3$ PSCs. Moreover, the feasibility of the single-homojunction PSC without an HTL and an ETL for highly efficient PSCs is worth further study.

Stability of the homojunction films and solar cells

To study the stability of the homojunction, transmission electron microscope (TEM) studies are carried out to investigate the possible ion diffusion issue in the grain boundaries between the p-type and n-type perovskite layers. The whole PSC is cross-sectioned by means of a focused ion beam (FIB). Figure 6a–d shows the cross-sectional PSCs of the standard p–i–n structure and the homojunction structure, respectively. The interface between the p-type and n-type perovskite layers is clearly visible as a neat boundary. To verify the stability of the homojunction, we store the homojunction PSC without encapsulation in ambient air under dark conditions for 160 h. In Fig. 6e,f, the interface between the p-type and n-type perovskite layers is still clearly visible after 160 h of storage compared with the fresh condition. Moreover, we mark the p-type perovskite layer with bromide and employ TEM with energy-dispersive X-ray analysis to inspect the ion migration in the homojunction (Supplementary Fig. 20). We note that little or no ion migration between the two types of perovskite layer after the PSC was measured under AM1.5 illumination and stored for 160 h. Therefore, the results suggest that the homojunction with self-doped perovskite layers is a stable structure under the conditions investigated.

The long-term stability of PSCs is studied to evaluate the effects of the homojunction. We examine the performance of unencapsulated PSCs stored in ambient air (25 °C and 40 ± 10% relative humidity) under dark conditions for 792 h. As shown in Fig. 6g, the evolution of the PCE over time reveals a similar trend for PSCs with and without the homojunction. The result shows that the PCE of a $MAPbI_3$ homojunction PSC decreased from 20.27% to 19.56%, which maintained 96% of the initial PCE after 792 h, whereas the PCE of a $MAPbI_3$ standard p–i–n PSC maintained 94% of the initial PCE (from 17.39% to 16.29%). This indicates that the homojunction PSCs are relatively stable even in the presence of moisture and oxygen, which are known to be critical factors in perovskite degradation. The $FA_{0.15}MA_{0.85}PbI_3$ homojunction PSC shows a marginal decrease in PCE, from 21.23% to 20.66%, after 792 h, thus retaining 97% of the initial PCE (other parameters shown in Supplementary Fig. 21). Hence, it is clear that the as-fabricated PSCs with the homojunction possess excellent long-term stability, which can be ascribed to the fact that the large grains of the n-type perovskite layer and the film compactness of the p-type perovskite layer can minimize the negative impact of oxygen and moisture.

Conclusions

In summary, we have demonstrated a perovskite homojunction structure to enhance the performance of planar PSCs using a p-type perovskite/n-type perovskite bilayer fabricated by a combined deposition method. The formation of the p–n junction in the homojunction structure has been verified by cross-sectional

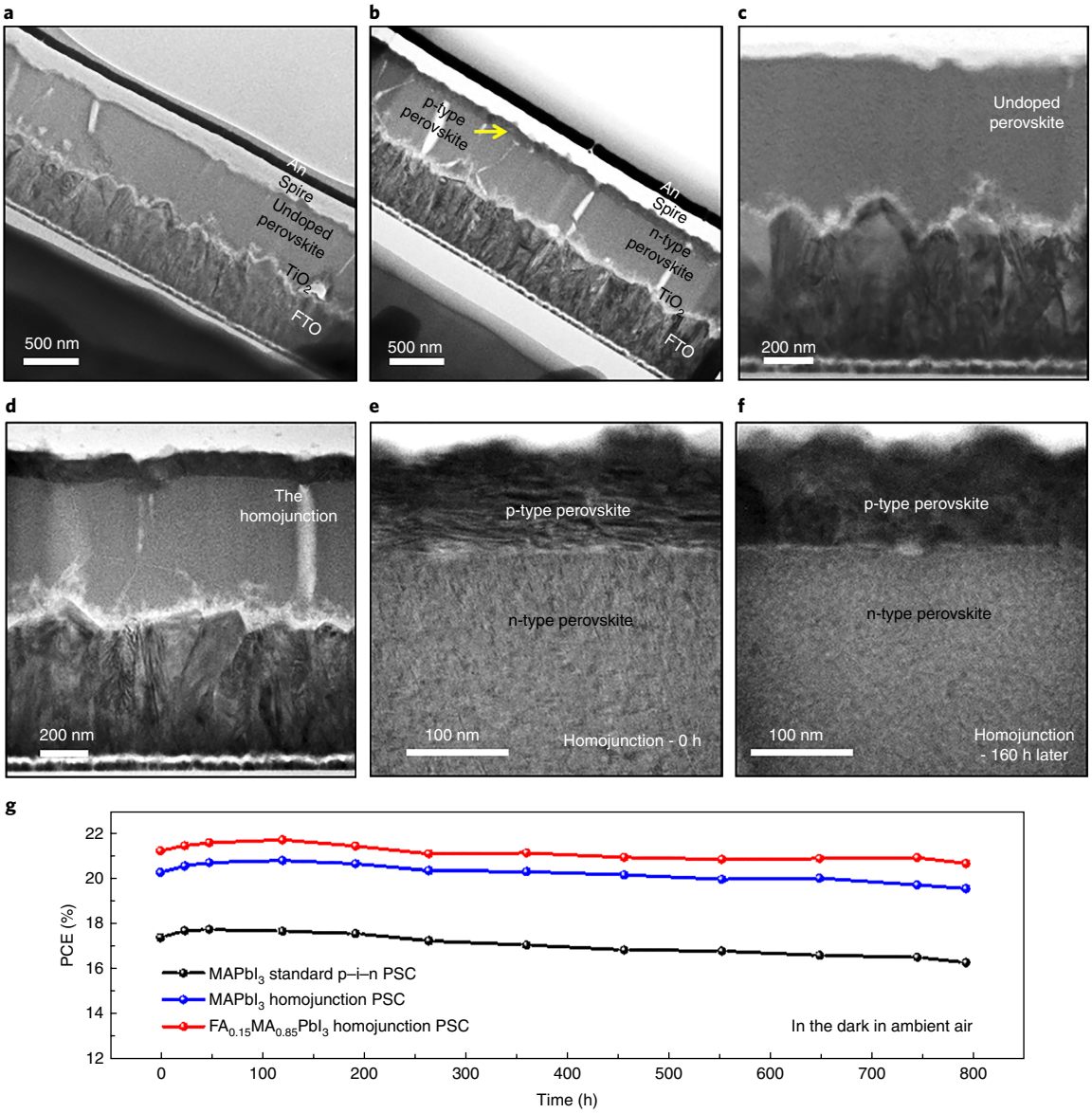

Fig. 6 | The perovskite film analysis and stability assessment of the standard p–i–n PSC and the homojunction PSC. a,**b**, Cross-sectional TEM images of the standard p–i–n PSC (**a**) and the homojunction PSC (**b**). **c**,**d**, Local cross-sectional TEM images of the undoped perovskite (**c**) and the homojunction (**d**). **e**,**f**, Cross-sectional TEM images of the fresh (0 h; **e**) and 160 h-later (store at 25 °C and ~40% relative humidity; **f**) homojunction structures, respectively. **g**, Evolution of PCE relative to the initial parameters for PSCs without encapsulation stored in ambient air under dark conditions.

KPFM measurements under a series of bias voltages. The planar homojunction PCSs show an enhanced PCE with respect to standard p–i–n PSCs as a consequence of oriented charge transport and reduced carrier recombination. A certified efficiency exceeding 20% is achieved in the $MAPbI_3$ homojunction PSCs. Furthermore, $FA_{0.15}MA_{0.85}PbI_3$ homojunctions are investigated and integrated into PSCs, enabling efficiencies of up to 21.38%. This work demonstrates that the perovskite homojunction is a valid alternative approach to the p–i–n traditional heterojunction PSCs for fabricating highly efficient PSCs.

Methods

Preparation of the perovskite homojunction. The perovskite homojunction is formed by n-type and p-type perovskite layers. To fabricate the n-type perovskite layer, a one-step spin-coating method was used as in previous published papers[39,40]. To prepare the perovskite precursor solution, 159 mg MAI (Xi'an Polymer Light Technology Corp.), and 462 mg 1.0 M, 485 mg 1.05 M, 508 mg 1.1 M and 531 mg 1.15 M PbI_2 were mixed in anhydrous dimethylformamide/dimethylsulphoxide (600 mg/78 mg) solution (Sigma-Aldrich, 99.8%), which was stirred at room temperature in a glove box. It was spin-coated directly on FTO/compact TiO_2 substrate at 4,000 r.p.m. for 30 s. During the spin-coating step, 0.5 ml of diethyl ether was poured on the surface at 25 s before the end. The light-yellow transparent films were converted into brownish-red perovskite films by heating at 130 °C for 5 min. From this process, n-type perovskite films with various doping concentrations were obtained with PbI_2/MAI ratios of 1, 1.05, 1.10 and 1.15. For depositing the p-type perovskite film on the n-type film, a new formation method combining evaporating and dipping processes was developed. PbI_2 films with thicknesses of 10 nm, 20 nm, 40 nm, 60 nm and 80 nm were evaporated directly on the surface of n-type perovskite films, respectively. Then, these films were dipped in 40 mg ml^{-1} MAI/isopropanol solution. After rinsing with isopropanol (Sigma-Aldrich), the prepared films were heated at 100 °C. We chose a PbI_2 thickness of 60 nm followed by a dipping time of 60 s, whose precursor ratio is measured at ~0.91 (PbI_2/MAI). Then the perovskite homojunction formed by n-type and p-type perovskite films was obtained through the above process.

PSC fabrication. FTO glass substrates were cleaned by dust-free paper first, and then washed with deionized water, ethanol and acetone twice. Then the FTO substrates were dried by blowing with high-purity nitrogen. A compact TiO_2 layer

with a thickness of approximately 20 nm was fabricated on FTO by $TiCl_4$ treatment at 70 °C for 60 min as shown in previous papers[29,39,46]. After drying in a drying oven at 50 °C for 2 h, the perovskite homojunction was deposited directly on these substrates by the process mentioned above. The hole transport layer (150 nm) was obtained by spin-coating the 2,20,7,70-tetrakis[*N*,*N*-di(4-methoxyphenyl) amino]-9,90-spirobifluorene (spiro-OMeTAD) solution (80 mg ml^{-1} dissolved in chlorobenzene, Xi'an Polymer Light Technology Corp.) with the standard additives tertbutylpyridine (28.5 µl in 1 ml chlorobenzene) and lithiumbis-(trifluoromethanesulfonyl) imide (8.75 mg ml^{-1}) at a speed of 4,000 r.p.m. for 30 s in a glove box, followed by oxidation in clean air for 6 h. After that, the Au electrode with a thickness of 100 nm was prepared by the vacuum evaporation equipment.

Perovskite film characterization. The morphologies of the as-prepared $MAPbI_3$ films were characterized by SEM (Hitachi S-4800). The chemical compositions and structures of the perovskite films were analysed by X-ray diffraction (Bruker D8 Advance X-ray diffractometer, Cu-Kα radiation $\lambda = 0.15406$ nm). The valence spectra were measured by XPS (ESCSLAB 250Xi). All spectra were shifted to account for sample charging using inorganic carbon at 284.80 eV as a reference. The static PL spectra of the perovskite films on FTO substrates were measured by an Edinburgh PLS 980. TRPL decay was measured using a transient-state spectrophotometer (Edinburgh Ins. F900) under the irradiation of a 485 nm pulse laser.

Hall. The sample was characterized using a Nanometrics HL5500 Hall System. An 80 nm gold layer was thermally evaporated onto the perovskite films to serve as metal contacts. All of the measurements were performed at room temperature (25 °C) and aphotic conditions. Other condition parameters are as follows: the current measuring range is 10 pA (d.c.), and the magnetic field is 0.503 T.

PSC characterization. Current–voltage curves were measured using a source meter (Keithley 2400) under AM1.5G irradiation with a power density of 100 mW cm^{-2} from a solar simulator (XES-301S+EL-100) by forward (−0.1 V to 1.2 V) or reverse (1.2 V to −0.1 V) scans. The step voltage was fixed at 12 mV and the delay time was set at 10 ms. The light intensity was calibrated by a standard silicon cell (the KG-5 mono-Si cell). All of the PSCs had no encapsulation and were tested in ambient air (25 °C, ~40% humidity) and employed a mask with an aperture area of 0.07 cm^2. The EQE was measured using QE-R systems (Enli Tech.).

PSC simulation. PSC simulation was carried out using wxAMPS software, based on the standard p–i–n PSC, FTO/TiO_2 (20 nm)/undoped perovskite (540 nm)/spiro-OMeTAD (200 nm)/Au, and the homojunction PSC, FTO/TiO_2 (20 nm)/n-type perovskite (480 nm)/p-type perovskite (60 nm)/spiro-OMeTAD (200 nm)/Au. The doping concentrations, mobility and other properties of the materials are reported in Supplementary Tables 3 and 4.

AFM and KPFM. The surface AFM and KPFM were carried out using an Agilent SPM 5500 with the sample chamber filled with high-purity N_2. The cross-sectional AFM and KPFM were carried out using an Asylum Research MFP3d with the sample chamber filled with high-purity N_2. For the cross-sectional KPFM measurements, the devices were cleaved to expose the cross-section from the film side, and no further treatment. We cut a notch at the side of the substrate (outside the active area of the solar cells) using a diamond cutter, and fractured the device by tension rather than by compression to expose the cross-section. The sample was fixed in a custom-made vertical sample holder with electrical connections to both electrodes. The FTO layer of the device was grounded. The measurement was carried out in the dark.

The potential images were recorded in tapping mode using a conductive PtSi-FM probe (NANOSENSORS, Pt-coated Si with a frequency of ~75 KHz and a nominal tip radius of ~25 nm). Amplitude-modulation KPFM measurements were carried out. The contact potential difference (CPD) between the probe and the sample was measured simultaneously with the topographic signal by the single-pass mode. The CPD signals reflect the potential distribution of the sample surface, as the workfunction of the probe is constant during the measurement. The topographic height was obtained by maintaining the amplitude of the first cantilever resonance (~71 kHz). To separate topographic from CPD signals, increase the accuracy and minimize probe convolution effects, the a.c. electrostatic force component was generated at the second resonance (~420 kHz) of the cantilever by applying a small a.c. voltage of 0.5 V. The scan rate was 0.6 Hz.

KPFM measurements were performed under different bias voltages (V_b) from +0.5 to −1.0 V on the same area of the cross-section of the device. The V_b was applied to the device using a Keithley 2400 source meter. The ion migration had no significant effect on the potential distributions during the KPFM scanning with the V_b from −1 V to +0.5 V within 20 min. We applied the V_b for 2 min, and then started testing for a stable result. The electric field profiles were obtained by taking the first derivative of the potential profiles. As a small change in noise level potential would tremendously enhance the electric field profiles, the raw data must be smoothed before taking the derivative.

TEM. The cross-sectional morphologies of the full cells and interface characterization of the homojunction were investigated using a high-resolution TEM. The samples were prepared by vertical etching using FIB equipment (FEI Helios Nanolab 600i). The cross-sectional surface was in situ-coated with platinum using an FEI gas injection system to protect the surface from damage during FIB milling. A cross-sectional specimen approximately 80 nm in thickness was obtained. Then the images were obtained using a high-resolution TEM (FEI Titan G2) at an acceleration voltage of 300 kV.

Reporting Summary. Further information on research design is available in the Nature Research Reporting Summary linked to this article.

Data availability

The data that support the plots within this paper and other findings of this study are available from the corresponding author upon reasonable request.

Received: 26 March 2017; Accepted: 21 December 2018;
Published online: 4 February 2019

References

1. Yang, W. S. et al. High-performance photovoltaic perovskite layers fabricated through intramolecular exchange. *Science* **348**, 1234–1237 (2015).
2. Li, X. et al. A vacuum flash-assisted solution process for high-efficiency large-area perovskite solar cells. *Science* **353**, 58–62 (2016).
3. Saliba, M. et al. Incorporation of rubidium cations into perovskite solar cells improves photovoltaic performance. *Science* **354**, 206–209 (2016).
4. Cho, K. T. et al. Highly efficient perovskite solar cells with a compositionally engineered perovskite/hole transporting material interface. *Energy Environ. Sci.* **10**, 21–627 (2017).
5. Yang, W. S. et al. Iodide management in formamidinium-lead-halide–based perovskite layers for efficient solar cells. *Science* **356**, 1376–1379 (2017).
6. Kojima, A., Teshima, K., Shirai, Y. & Miyasaka, T. Organometal halide perovskites as visible-light sensitizers for photovoltaic cells. *J. Am. Chem. Soc.* **131**, 6050–6051 (2009).
7. Best Research-Cell Efficiencies Rev. 01-03-2019 (NREL, 2019); https://www.nrel.gov/pv/assets/pdfs/pv-efficiency-chart.20190103.pdf
8. Anyi, M. et al. A hole-conductor-free, fully printable mesoscopic perovskite solar cell with high stability. *Science* **345**, 295–298 (2014).
9. Fu, F. et al. Low-temperature-processed efficient semi-transparent planar perovskite solar cells for bifacial and tandem applications. *Nat. Commun.* **6**, 8932 (2015).
10. Johnston, M. B. & Herz, L. M. Hybrid perovskites for photovoltaics: charge-carrier recombination, diffusion,and radiative efficiencies. *Acc. Chem. Res.* **49**, 146–154 (2016).
11. Stranks, S. D. et al. Electron–hole diffusion lengths exceeding 1 micrometer in an organometal trihalide perovskite absorber. *Science* **342**, 341–344 (2013).
12. Dong, Q. et al. Electron–hole diffusion lengths > 175 µm in solution-grown $CH_3NH_3PbI_3$ single crystals. *Science* **347**, 967–970 (2015).
13. Green, M. A., Jiang, Y., Soufiani, A. M. & Ho-Baillie, A. Optical properties of photovoltaic organic–inorganic lead halide perovskites. *J. Phys. Chem. Lett.* **6**, 4774–4785 (2015).
14. Shi, D. et al. Low trap-state density and long carrier diffusion in organolead trihalide perovskite single crystals. *Science* **347**, 519–522 (2015).
15. Miyata, A. et al. Direct measurement of the exciton binding energy and effective masses for charge carriers in organic–inorganic tri-halide perovskites. *Nat. Phys.* **11**, 582–587 (2015).
16. Jeon, N. J. et al. Solvent engineering for high-performance inorganic–organic hybrid perovskite solar cells. *Nat. Mater.* **13**, 897–903 (2014).
17. Chen, H. N. et al. Solvent engineering boosts the efficiency of paintable carbon-based perovskite solar cells to beyond 14%. *Adv. Energy Mater.* **6**, 1502087 (2016).
18. Ahn, N. et al. Highly reproducible perovskite solar cells with average efficiency of 18.3% and best efficiency of 19.7% fabricated via Lewis base adduct of lead(II) iodide. *J. Am. Chem. Soc.* **137**, 8696–8699 (2015).
19. Jeon, N. J. et al. Compositional engineering of perovskite materials for high-performance solar cells. *Nature* **517**, 476–480 (2015).
20. Yang, Z. et al. Effects of formamidinium and bromide ion substitution in methylammonium lead triiodide toward high-performance perovskite solar cells. *Nano Energy* **22**, 328–337 (2016).
21. Kim, H. S. et al. Lead iodide perovskite sensitized all-solid-state submicron thin film mesoscopic solar cell with efficiency exceeding 9%. *Sci. Rep.* **2**, 591 (2012).
22. Liu, M., Johnston, M. B. & Snaith, H. J. Efficient planar heterojunction perovskite solar cells by vapour deposition. *Nature* **501**, 395–398 (2013).
23. Chiang, C. H. & Wu, C. G. Bulk heterojunction perovskite–PCBM solar cells with high fill factor. *Nat. Photon.* **10**, 196–200 (2016).
24. Son, D. Y. et al. Self-formed grain boundary healing layer for highly efficient $CH_3NH_3PbI_3$ perovskite solar cells. *Nat. Energy* **1**, 16081 (2016).
25. Bi, D. et al. Polymer-templated nucleation and crystal growth of perovskite films for solar cells with efficiency greater than 21%. *Nat. Energy* **1**, 16142 (2016).

26. Zheng, X. et al. Defect passivation in hybrid perovskite solar cells using quaternary ammonium halide anions and cations. *Nat. Energy* **2**, 2017102 (2017).
27. Jiang, Q. et al. Enhanced electron extraction using SnO_2 for high-efficiency planar-structure $HC(NH_2)_2PbI_3$-based perovskite solar cells. *Nat. Energy* **2**, 16177 (2016).
28. Burschka, J. et al. Sequential deposition as a route to high-performance perovskite-sensitized solar cells. *Nature* **499**, 316–319 (2013).
29. Wei, D. et al. TiO_2 embedded structure for perovskite solar cells with anomalous grain growth and effective electron extraction. *J. Mater. Chem. A* **5**, 1406–1414 (2016).
30. Wang, K., Liu, C., Du, P., Zheng, J. & Gong, X. Bulk heterojuntion perovskite hybrid solar cells with large fill-factor. *Energy Environ. Sci.* **8**, 1245–1255 (2015).
31. Ye, S. et al. A strategy to simplify the preparation process of perovskite solar cells by co-deposition of a hole-conductor and a perovskite layer. *Adv. Mater.* **28**, 9648–9654 (2016).
32. Wu, Y. et al. Perovskite solar cells with 18.21% efficiency and area over 1 cm^2 fabricated by heterojunction engineering. *Nat. Energy* **1**, 16148 (2016).
33. Kim, J., Lee, S. H., Lee, J. H. & Hong, K. H. The role of intrinsic defects in methylammonium lead iodide perovskite. *J. Phys. Chem. Lett.* **5**, 1312–1317 (2014).
34. Yin, W. J., Shi, T. & Yan, Y. Unusual defect physics in $CH_3NH_3PbI_3$ perovskite solar cell absorber. *Appl. Phys. Lett.* **104**, 063903 (2014).
35. Wang, Q. et al. Qualifying composition dependent p and n self-doping in $CH_3NH_3PbI_3$. *Appl. Phys. Lett.* **105**, 163508 (2014).
36. Lyubov, A. F., Nadezhda, N. D. & Pavel, A. T. The chemical origin of the p-type and n-type doping effects in the hybrid methylammonium-lead iodide ($MAPbI_3$) perovskite solar cells. *Chem. Commun.* **51**, 14917 (2015).
37. Benedikt, D. Perovskite–perovskite homojunctions via compositional doping. *J. Phys. Chem. Lett.* **9**, 2770–2775 (2018).
38. Ran, C., Xu, J., Gao, W., Huang, C. & Dou, S. Defects in metal triiodide perovskite materials towards high-performance solar cells: origin, impact, characterization, and engineering. *Chem. Soc. Rev.* **47**, 4581–4610 (2018).
39. Song, D. et al. Managing carrier lifetime and doping property of lead halide perovskite by postannealing processes for highly efficient perovskite solar cells. *J. Phys. Chem. C* **119**, 22812–22819 (2015).
40. Cui, P. et al. Highly efficient electron-selective layer free perovskite solar cells by constructing effective p–n heterojunction. *Solar RRL* **1**, 1600027 (2017).
41. Mali, S. S. & Hong, C. K. p–i–n/n–i–p type planar hybrid structure of highly efficient perovskite solar cells towards improved air stability: synthetic strategies and the role of p-type hole transport layer (HTL) and n-type electron transport layer (ETL) metal oxides. *Nanoscale* **8**, 10528–10540 (2016).
42. Miyano, K., Tripathi, N., Yanagida, M. & Shirai, Y. Lead halide perovskite photovoltaic as a model p–i–n diode. *Acc. Chem. Res.* **49**, 303–310 (2016).
43. Gil-Escrig, L., Miquel-Sempere, A., Sessolo, M. & Bolink, H. J. Mixed iodide-bromide methylammonium lead perovskite-based diodes for light emission and photovoltaics. *J. Phys. Chem. Lett.* **6**, 3743–3748 (2015).
44. Sessolo, M., Momblona, C., Gil-Escrig, L. & Bolink, H. J. Photovoltaic devices employing vacuum-deposited perovskite layers. *MRS Bull.* **40**, 660–666 (2015).
45. Liu, Y., Sun, Y. & Rockett, A. A new simulation software of solar cells—wxAMPS.*Sol. Energy Mater. Sol. C* **98**, 124–128 (2012).
46. Song, D. et al. Dual function interfacial layer for highly efficient and stable lead halide perovskite solar cells. *J. Mater. Chem. A* **4**, 6091–6097 (2016).
47. Bergmann, V. W. et al. Real-space observation of unbalanced charge distribution inside a perovskite-sensitized solar cell. *Nat. Commun.* **5**, 5001 (2014).
48. Jiang, C. S. et al. Carrier separation and transport in perovskite solar cells studied by nanometre-scale profiling of electrical potential. *Nat. Commun.* **6**, 8397 (2015).
49. Xiao, C. et al. Junction quality of SnO_2-based perovskite solar cells investigated by nanometer-scale electrical potential profiling. *ACS Appl. Mater. Interfaces* **9**, 38373 (2017).

Acknowledgements

This work is supported partially by the National Natural Science Foundation of China (grant no. 51772096), the Natural Science Foundation of Beijing Municipality (L172036), Joint Funds of the Equipment Pre-Research and Ministry of Education (6141A020225), the Par-Eu Scholars Program, the Science and Technology Beijing 100 Leading Talent Training Project, the Beijing Municipal Science and Technology Project (Z161100002616039), the Fundamental Research Funds for the Central Universities (2016JQ01 and 2017ZZD02) and the NCEPU `Double First-Class' Graduate Talent Cultivation Program. We thank Z. Cheng, R. Xu and Z. Liu for KPFM measurements and analysis, and X. Han and Z. Li for high-resolution TEM measurements. P.C. acknowledges the scholarship from the China Scholarship Council and thanks G. Cao for fruitful discussions.

Author contributions

M.L. supervised the project. P.C. and M.L. conceived and designed the experiments. P.C. and D.W. performed the main experiments and characterization, and wrote the manuscript. J.J. helped with device optimization and fabrication. H.H. helped with KPFM measurements. E.J. performed Hall measurements and analysed the data. T.W. performed the simulation with wxAMPs. P.C., D.W., J.J., H.H., E.J., S.D., T.W., W.W. and M.L. contributed to the data analysis, discussed the results and commented on the manuscript.

Competing interests

The authors declare no competing interests.

Additional information

Supplementary information is available for this paper at https://doi.org/10.1038/s41560-018-0324-8.

Reprints and permissions information is available at www.nature.com/reprints.

Correspondence and requests for materials should be addressed to M.L.

Publisher's note: Springer Nature remains neutral with regard to jurisdictional claims in published maps and institutional affiliations.

nature research

Corresponding author(s): Meicheng Li

Solar Cells Reporting Summary

Nature Research wishes to improve the reproducibility of the work that we publish. This form is intended for publication with all accepted papers reporting the characterization of photovoltaic devices and provides structure for consistency and transparency in reporting. Some list items might not apply to an individual manuscript, but all fields must be completed for clarity.

For further information on Nature Research policies, including our data availability policy, see Authors & Referees.

Experimental design

Please check: are the following details reported in the manuscript?

1. Dimensions

Area of the tested solar cells	☒ Yes	The active area was 0.1 cm2, which is a rectangle (0.2cm*0.5cm).
	☐ No	*Explain why this information is not reported/not relevant.*
Method used to determine the device area	☒ Yes	Optical Microscope.
	☐ No	*Explain why this information is not reported/not relevant.*

2. Current-voltage characterization

Current density-voltage (J-V) plots in both forward and backward direction	☒ Yes	We provide hysteresis scans in Figure 5 and Supplementary Figures 16.
	☐ No	*Explain why this information is not reported/not relevant.*
Voltage scan conditions *For instance: scan direction, speed, dwell times*	☒ Yes	The voltage scan conditions: forward (-0.1V to 1.2V) and reverse (1.2V to -0.1V), 0.012V/step, 10 ms delay.
	☐ No	*Explain why this information is not reported/not relevant.*
Test environment *For instance: characterization temperature, in air or in glove box*	☒ Yes	The test environment: 25 °C, 30%-40% humidity in ambient air. All of the devices have no encapsulation.
	☐ No	*Explain why this information is not reported/not relevant.*
Protocol for preconditioning of the device before its characterization	☒ Yes	No preconditioning protocol was used.
	☐ No	*Explain why this information is not reported/not relevant.*
Stability of the J-V characteristic *Verified with time evolution of the maximum power point or with the photocurrent at maximum power point; see ref. 7 for details.*	☒ Yes	We provide maximum power point tracking data in Figure 5 as well as stabilized certified efficiencies in the Supplementary Figure 14. In addition, we performed long-term (up to 792hours) efficiency tracking of the PSCs in air (Figure 6 and Supplementary Figures 20).
	☐ No	*Explain why this information is not reported/not relevant.*

3. Hysteresis or any other unusual behaviour

Description of the unusual behaviour observed during the characterization	☒ Yes	No unusual behaviour was observed and no significant hysteresis (about 0.7% change in efficiency in forward or backward scan for the homojunction PSCs).
	☐ No	*Explain why this information is not reported/not relevant.*
Related experimental data	☒ Yes	We provide hysteresis scans in Figure 5 and Supplementary Figures 16.
	☐ No	*Explain why this information is not reported/not relevant.*

4. Efficiency

External quantum efficiency (EQE) or incident photons to current efficiency (IPCE)	☒ Yes	Yes, the EQE data for the devices have been provided as shown in Supplementary Figure 13 and 18.
	☐ No	*Explain why this information is not reported/not relevant.*
A comparison between the integrated response under the standard reference spectrum and the response measure under the simulator	☒ Yes	The integrated short-circuit current from the EQE spectrum matches the short-circuit current from the JV scan (of masked cells) within the setup measurement error of about 2%.
	☐ No	*Explain why this information is not reported/not relevant.*

For tandem solar cells, the bias illumination and bias voltage used for each subcell	☐ Yes ☒ No	*State where this information can be found in the text.* N.A.

5. Calibration

Light source and reference cell or sensor used for the characterization	☒ Yes ☐ No	The light source: the solar simulator (XES-301S+EL-100) with standard AM 1.5G irradiation (100mW·cm-2). The reference cell: the KG-5 mono-Si cell. *Explain why this information is not reported/not relevant.*
Confirmation that the reference cell was calibrated and certified	☒ Yes ☐ No	Yes, the reference cell was certified by the National Institute of Metrology of China. *Explain why this information is not reported/not relevant.*
Calculation of spectral mismatch between the reference cell and the devices under test	☐ Yes ☒ No	*State where this information can be found in the text.* The light spectrum used in measurement is match with the reference silicon cell, and we have not calculated the spectral mismatch between the reference cell and the tested devices.

6. Mask/aperture

Size of the mask/aperture used during testing	☒ Yes ☐ No	A mask with an aperture area of 0.07 cm2 was used for measurements. *Explain why this information is not reported/not relevant.*
Variation of the measured short-circuit current density with the mask/aperture area	☒ Yes ☐ No	There is no obvious change in the measured short-circuit current density with or without masks. *Explain why this information is not reported/not relevant.*

7. Performance certification

Identity of the independent certification laboratory that confirmed the photovoltaic performance	☒ Yes ☐ No	The National Institute of Metrology of China *Explain why this information is not reported/not relevant.*
A copy of any certificate(s) *Provide in Supplementary Information*	☒ Yes ☐ No	Certified measurements are shown in Supplementary Figures 14. *Explain why this information is not reported/not relevant.*

8. Statistics

Number of solar cells tested	☒ Yes ☐ No	There are more than 90 MAPbI3-based PSCs (with or without the homojunction structure) have been test. *Explain why this information is not reported/not relevant.*
Statistical analysis of the device performance	☒ Yes ☐ No	A statistical analysis of the performance has been included in Figure 5 and Supplementary Figure 15 and 17. *Explain why this information is not reported/not relevant.*

9. Long-term stability analysis

Type of analysis, bias conditions and environmental conditions *For instance: illumination type, temperature, atmosphere humidity, encapsulation method, preconditioning temperature*	☒ Yes ☐ No	The long-term stability of PSCs is studied under AM 1.5G irradiation in air. We examine the performance of unencapsulated PSCs stored in ambient air (25 °C and 40±10 % RH) under dark conditions for 792 hours. *Explain why this information is not reported/not relevant.*